

# EFFECTS OF SURFACE ROUGHNESS TOPOGRAPHY IN DEVELOPED AND TRANSIENT CHANNEL FLOWS

Junlin Yuan

Department of Mechanical Engineering  
Michigan State University  
428 S. Shaw Ln., East Lansing, MI, 48824  
junlin@egr.msu.edu

## ABSTRACT

The role of roughness topographies on turbulence intensity and coherence and their responses to non-equilibrium, accelerating flows are investigated through direct numerical simulations of developed and transient channel flows. Two rough surfaces different in surface length-scale spectrum are compared; they are resolved in the simulations using an immersed boundary method. Results indicate that the topographical length scales larger than the boundary layer thickness may directly affect outer-layer energetic turbulent motions with sizes of the same order, while, inside the wall region, these turbulent motions are less sensitive to the largest surface scales due to scale separation. In non-equilibrium flows, it is observed that the roughness topography plays an important role in determining the turbulence response in the roughness sublayer, especially during the initial response.

## INTRODUCTION

To formulate rational turbulence closures for engineering flow simulations where the surface roughness is not resolved, it is necessary to understand the roughness effects on turbulence velocity scale ( $\sqrt{k}$ , where  $k$  is turbulent kinetic energy, TKE), time scale ( $\tau = k/\varepsilon$ , where  $\varepsilon$  is TKE dissipation rate) and length scale. The traditional approach to model the effects of an arbitrary roughness on turbulence is to use the earlier measurements on equilibrium flows over uniform sand grains (Nikuradse, 1933) to establish correlations between roughness heights (quantified in terms of peak-to-trough height,  $k_c$ , first-order moment,  $Ra$ , second-order moment,  $k_{rms}$ , etc.) and the turbulence scales at the lower boundary of the outer layer. This is done by relating the physical roughness scales to a single length,  $k_s$  (the equivalent sand-grain height used to quantify the momentum deficit on rough walls) as a middle step;  $k_s$  is then used to predict the turbulent scales, with the assumption that such correlations apply also to other roughness geometries and other flow states (see, e.g., Wilcox (2006)).

Since it is possible that different turbulent scales near the wall are affected by different sets of the surface characteristics, a single length  $k_s$  may not be sufficient to characterize the effects of a realistic, multi-scale roughness topography on various turbulent scales. In addition, most previous studies on rough-wall, non-equilibrium flows are limited to relatively uniform roughness with a narrow range of length scales (Cal *et al.*, 2009; Yuan & Piomelli, 2014b,

2015), it is not clear how effects of realistic topographies are manifested in non-equilibrium flows.

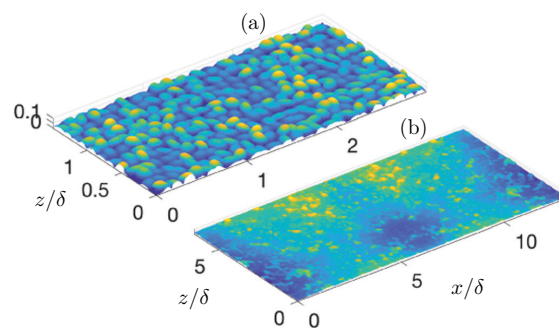


Figure 1. Surfaces colored by height. (a) one quarter of SG surface (zoomed in). (b) one half of TB surface.

## OBJECTIVES

Two questions are investigated. (1) In an equilibrium wall-bounded flow, are various turbulent scales affected by the roughness geometry in different ways? (2) In a non-equilibrium flow, is the turbulence response affected by not only the presence of roughness, but also its texture? Here, the two flow states are achieved as either a fully developed channel or an accelerating transient channel. Compared to previous studies of non-equilibrium, rough-wall flows with spatial acceleration, a transient channel flow provides the advantage of being able to include larger horizontal scales of roughness texture for the same level of mean distortion. Two surfaces from different origins are compared: one synthetic sand-grain roughness, “SG” (Figure 1a), and one replicated from a surface scan on a hydraulic turbine blade, “TB” (Figure 1b). Directional numerical simulations (DNS) are performed with the roughness geometry well resolved using an immersed boundary method (IBM).

## METHODOLOGY

The incompressible flow of a Newtonian fluid is governed by the equations of conservation of mass and momen-

Table 1. Case summary. SM: smooth; SG: sand grain; TB: turbine roughness.  $n_i, n_j, n_k$  are number of grid in  $x, y, z$ . Legends in following figures: — SG, --- TB, - - - SM.

Surface	$Re_{b1}$	$Re_{b2}$	$Re_\tau$	$Ra/\delta$	$k_c/\delta$	$k_s^+$	$(n_i, n_j, n_k)$	$(\Delta x^+, \Delta y^+(1), \Delta z^+)$
SM	20,000	–	1000	0	0	0	(512, 256, 512)	(11.7, 0.3, 5.8)
SG	12,000	–	1000	0.014	0.09	60	(512, 236, 256)	(11.0, 0.7, 11.0)
TB	14,221	–	1000	0.014	0.13	24	(1024, 259, 1024)	(13.0, 0.8, 13.0)
SM	3,000	9,000	189–498	0	0	0	(512, 100, 256)	(4–12, 0.1–0.3, 2–6)
SG	3,000	9,000	270–814	0.019	0.12	21–80	(256, 236, 128)	(6–19, 0.2–0.6, 6–19)
TB	3,000	9,000	231–695	0.019	0.17	7.5–18.7	(512, 273, 512)	(8–24, 0.1–0.3, 8–16)

tum:

$$\frac{\partial u_i}{\partial x_i} = 0, \quad (1)$$

$$\frac{\partial u_j}{\partial t} + \frac{\partial u_i u_j}{\partial x_i} = -\frac{\partial P}{\partial x_j} + \nu \nabla^2 u_j + F_j. \quad (2)$$

$x_1, x_2$  and  $x_3$  (or  $x, y$  and  $z$ ) are, respectively, the streamwise, wall-normal and spanwise directions, and  $u_j$  (or  $u, v$  and  $w$ ) are the velocity components in those directions;  $P = p/\rho$  is the modified pressure,  $\rho$  the density and  $\nu$  the kinematic viscosity. The term  $F_j$  in Equation (2) is a body force imposed by the IBM used to impose non-slip boundary conditions on the rough surface, which is well-resolved by the grid. The method is based on the volume-of-fluid approach (Scotti, 2006); its detailed implementation in the in-house fluid solver and validation are provided by Yuan & Piomelli (Yuan & Piomelli, 2014c,b). Specifically, the volume fraction occupied by the fluid,  $\phi(x, y, z)$ , of each grid cell is calculated in pre-processing, and used to calculate the force  $F_1(x, y, z)$ , at each time step, to decrease the momentum in each grid cell by a fraction of  $(1 - \phi)$ . The  $F_1$  values are non-negligible in the boundary cells of roughness, and are negligible inside roughness.  $F_1$  can be integrated in the wall-normal direction to obtain the total drag (i.e., wall shear stress  $\tau_w$ )—the sum of viscous and pressure components—at a  $(x, z)$  location on a surface.

The simulations are performed using a well-validated code that solves the governing equations (1) and (2) on a staggered grid using second-order, central differences for all terms, second-order accurate Adams-Bashforth semi-implicit time advancement, and MPI parallelization (Keating *et al.*, 2004).

In the roughness sublayer, roughness leads to spatial heterogeneity of the time-averaged variables; such time-averaged fluctuations require the double-averaging decomposition technique to be separated from turbulent fluctuations (Raupach & Shaw, 1982),

$$\theta(x, y, z, t) = \langle \bar{\theta} \rangle(y) + \tilde{\theta}(x, y, z) + \theta'(x, y, z, t).$$

where  $\theta$  is an instantaneous flow variable,  $\langle \theta \rangle$  is the intrinsic spatial average in the  $(x, z)$ -plane,  $\langle \theta \rangle = 1/A_f \int_{A_f} \theta dA$  (where  $A_f$  is the area occupied by fluid),  $\bar{\theta}$  denotes the temporal average,  $\theta'$  is the instantaneous turbulent fluctuations from  $\bar{\theta}$ , and  $\tilde{\theta} = \bar{\theta} - \langle \bar{\theta} \rangle$  is the dispersive (or wake) fluctuations.

Simulations are carried out on equilibrium and accelerating channel flows for three surfaces: smooth (SM), and both SG and TB roughnesses. The SG surface is formed as a uniform distribution of randomly oriented ellipsoids of the same geometry (Scotti, 2006); it is characterized by narrow length-scale variation. In contrast, the TB surface consists of a much wider spectrum of horizontal length scales, from the smallest ones resolvable by the grid, to scales larger than the boundary layer thickness. The initial turbine roughness scan is mirrored in both  $x$  and  $z$  to produce the final TB surface that satisfies the periodic condition. The two surfaces share the same first-order moment of height statistics ( $Ra/\delta$ , where  $\delta$  is the boundary layer thickness, i.e., channel half-height).

Parameters of all cases are listed in Table 1. The parameter space is designed to achieve the fully rough regime for both roughness geometries, in both developed channel and the later stage of the transient channels. The fully rough regime is desired since the ability of roughness to affect the flow (friction coefficient,  $k_s/Ra$ , etc.) is Reynolds-number-independent, a favorable simplification. Results of  $k_s^+$  show that the fully rough regime is indeed achieved, with the critical  $k_s^+$ —corresponding to the start of the fully rough regime—found as  $k_{s,cri}^+ \approx 60$  and 20 for SG and TB, respectively (Yuan & Piomelli, 2014a).

The domain sizes in  $x$  and  $z$  ranges from  $(6\delta, 3\delta)$  for SM and SG to  $(13\delta, 13\delta)$  for TB, where larger domain is required to accommodate larger horizontal scales. For transient channels, longer domain in  $x$  is used to allow for elongation of turbulent eddies during acceleration. For all cases, the grid size normalized by Kolmogorov length,  $\eta$ , is 6–11 in  $x$  and  $z$ , and much smaller in  $y$ , sufficient for resolving the dissipative scales.

For both channel flows, the flow is forced by a mean streamwise pressure gradient (constant in developed channels but varying in transient channels); the periodic boundary condition is applied in  $x$  and  $z$ . Data are collected for a simulation time  $T \approx 50\delta/u_\tau$  (where  $u_\tau$  is the friction velocity) after the transient period. For the transient channel flows, similar set-ups are applied as in He & Sedghi (2013). Strong temporal acceleration is achieved by imposing a temporally varying streamwise pressure gradient, which is constantly adjusted to produce a prescribed step jump of the mass flux value. To limit the computational cost, only a half channel is simulated, with symmetric boundary condition at the top boundary. The initial fully developed flow is simulated with  $Re_{b1} = U_{b1}\delta/\nu$  (where  $U_b$  is the instantaneous bulk velocity); then, at simulation

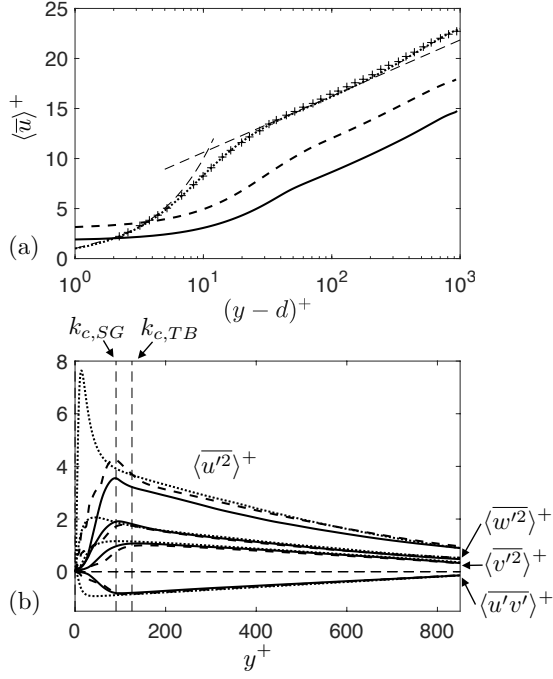


Figure 2. (a) Double-averaged velocity and (b) Reynolds stresses. + smooth-wall experiments (Schultz & Flack, 2013).

time  $t^* = tU_b/\delta = 0$ , the mass-flow rate is subject to a step increase (during a short time interval  $\Delta t u_{\tau,1}/\delta = 0.085$ ) to achieve  $Re_{b2} = 3Re_{b1}$ , and the flow is allowed to accelerate till a new equilibrium is reached. The acceleration is strong enough to cause a departure from equilibrium for a period of  $\Delta t^* \approx 50$  above a smooth wall. For each case, the transient simulations are repeated, so that for each  $t^*$  after the step change around 200 snapshots are stored for statistics calculations at the corresponding  $t^*$ .

## RESULTS

### Fully Developed Channels

The mean velocity profiles are shown in Figure 2a, where  $d$  is the zero-plane displacement—obtained as the location of the centroid of the wall-normal profile of the averaged total drag distribution,  $F_1$  (Jackson, 1981)—and the superscript “+” indicates normalization in wall units ( $u_\tau$  and viscous length scale,  $\delta_\nu = \nu/u_\tau$ ). Although SG and TB surfaces produce the same average height,  $Ra$ , they yield significantly different values of roughness function,  $\Delta U^+$  (the offset of mean velocity in the logarithmic region from the smooth-wall profile); as a result, the ratio  $k_s/Ra$  for SG is three times as high as TB; this is consistent with Yuan & Piomelli (2014a), where it is shown that realistic turbine surfaces, with wider scale variation than uniform distributed roughness, tend to be less capable of producing drag, and tend to reach the fully rough regime at much lower  $k_s^+$  than regular roughness. In addition, a careful analysis to identify the logarithmic region as the region with constant value of  $(y-d)^+ \partial \langle \bar{u} \rangle^+ / \partial y^+$  (not shown) shows that the logarithmic regions lie between  $k_c$  and  $(y-d)^+ < 150$ .

The normal and shear components of the Reynolds stress tensor are shown in Figure 2b. Wall similarity is satisfied, and the thickness of the roughness sublayer—the layer in which the Reynolds stresses normalized by  $u_\tau^2$  are sur-

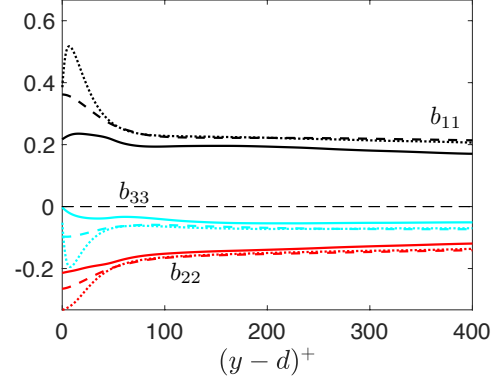


Figure 3. Reynolds stress anisotropy for all cases

face dependent—is around  $k_c$ . This also indicates that the turbulent velocity scale,  $\sqrt{k^+}$ , are similar for all three cases above the roughness sublayer.

To highlight the effects of roughness topography on turbulent fluctuations in the roughness sublayer, the anisotropy of the Reynolds stress tensor,

$$b_{\alpha\alpha} = \frac{\langle u'_\alpha u'_\alpha \rangle}{\langle u'_i u'_i \rangle} - \frac{1}{3}$$

is compared among the three cases. Again, outside the roughness sublayer the profiles are similar. But near the wall SG produces the most isotropic turbulent energy distribution among all three directions; in contrast, TB profiles tend towards the smooth-wall distributions, with the main difference being the non-negligible wall-normal and spanwise fluctuations at the virtual wall,  $y = d$ .

In rough-wall flows the dispersive stresses play a role in mean-momentum balance and turbulence generation in the roughness sublayer; their profiles are shown in Fig. 4. These stresses are non-negligible inside the roughness sublayer only. Significant differences are observed between SG and TB: (1) TB surface produces more anisotropic dispersive fluctuations, with much more dominant  $\langle \tilde{u}^2 \rangle$  than other normal components; (2) the shear component is significant in for SG, but negligible for TB.

To quantify the length scale of the energy-containing turbulent motions, one may use the integral length scale of the  $u'$  motions,

$$L_{11}(y) = \int_0^\infty R_{11,x}(y, \Delta x) d(\Delta x)$$

where  $R_{11,x}$  is the two-point autocorrelation of  $u'$  in the  $(x, z)$ -plane with the separation in  $x$ ,

$$R_{11,x}(y, \Delta x) = \frac{\langle u'(x, y, z, t) u'(x + \Delta x, y, z, t) \rangle}{\sigma(y)^2},$$

and  $\sigma$  is the root-mean-square deviation of  $u'$ . Likewise,  $G_{11}(y)$  is integral length obtained from  $R_{11,z}(y, \Delta z)$ , the two-point autocorrelation with separation in  $z$ . Fig. 5 compares the integral lengths in all three cases at various  $y$  locations above the roughness sublayer, for  $y - d = 0.05h$  to

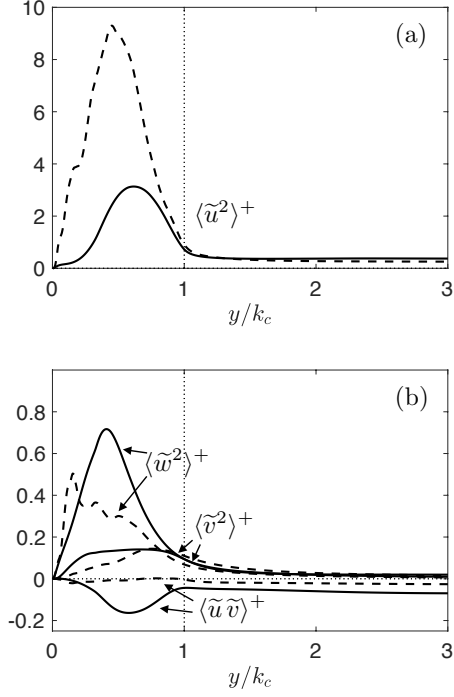


Figure 4. Double-averaged dispersive stresses.

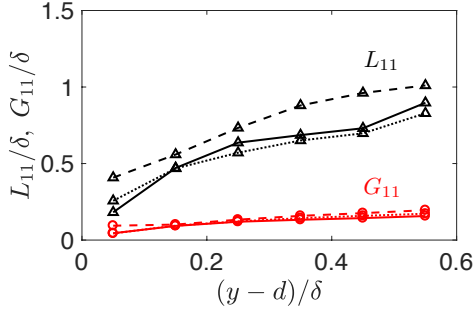


Figure 5. Integral length scale of  $u'$  motions in the outer layer.

0.55 $h$ . Longer streamwise correlation lengths are shown for case TB than for SM and SG, with roughly 60% higher values near the wall, and 20% higher in the middle of the boundary layer.

To explain the difference in integral lengths at the bottom of the outer layer, Fig. 6 compares the instantaneous  $u'$  in a  $(x, z)$  plane at  $(y-d)/\delta = 0.05$  in all cases. The length scales of the coherent meandering motions are similar in SM and SG, both of which relatively uniformly distributed. For TB, however, the  $u'$  intensity and coherence appear to be modulated by underlying roughness topography: more intense motions are observed in the relatively “open” regions where the roughness peaks are fewer or lower, while weaker  $u'$  fluctuations are found in the regions with (or between) high roughness peaks. The fact that SG does not lead to a significant change of outer-layer turbulence coherence may be because the surface heights can be considered homogeneously distributed, as its characteristic length scale—the separation between elements—is  $0.12\delta$ , small

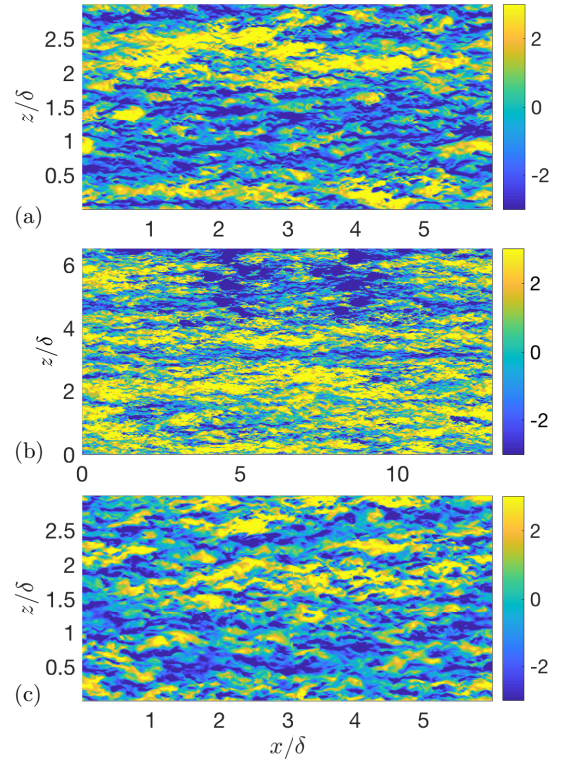


Figure 6. Contours of instantaneous  $u'^+$  at  $(y-d)/\delta = 0.05$  for (a) SM, (b) TB (one half is shown), (c) SG.

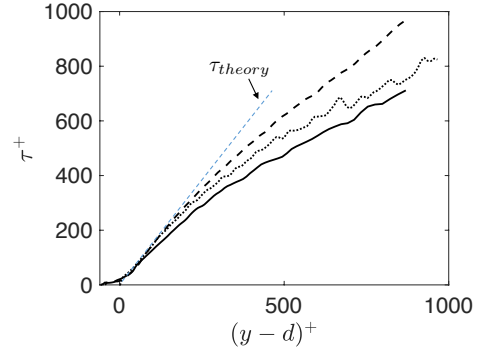


Figure 7. Comparison of turbulent time scale.

compared to the boundary layer thickness.

The turbulent time scale,  $\tau^+ = k^+/\varepsilon^+$  is compared in Fig. 7. In the logarithmic region,  $(y-d)^+ < 150$ , all three cases collapse well with the theoretical values in the logarithmic region,  $\tau_{theory}^+ = \kappa k / \langle u'v' \rangle (y-d)^+$ , which is obtained assuming logarithmic mean-velocity profile and local balance between shear production and viscous dissipation. Farther away from the wall, SG produces similar  $\tau^+$  values as the smooth case, while TB gives roughly 25% higher values of  $\tau^+$ , due to a lower  $\varepsilon^+$  value.

An interesting observation made by comparing various turbulent scales (Figs. 2b, 5, and 7) is that, in the logarithmic region, although TB leads to longer  $L_{11}$ , the time and velocity scales collapse for all cases, indicating that the integral scale may not be an appropriate quantification of the size of energetic turbulent motion for TB near the wall. It may be because  $L_{11}$  is strongly affected by surface heterogeneity of scales larger than  $\delta$ , independent from the size of the energetic, coherent turbulent motions—scaling with

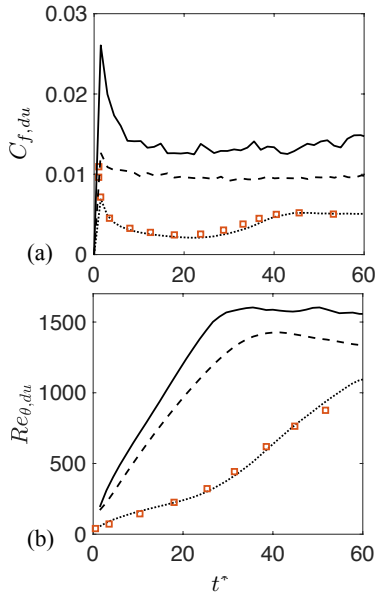


Figure 8. Boundary layer parameters of the differential flow in transient channels: (a) friction coefficient and (b) Reynolds number.  $\square$  DNS by He & Seddighi (2013).

the distance from the wall—with size of the order of  $0.1\delta$ . On the other hand, deeper into the outer layer, the longer integral length in TB coincides with longer time scale, indicating that the integral scale corresponds to the scale of the energetic motions, the size of which increases to the order of  $\delta$ .

### Transient channels

To find out whether the topographical effects play an important role in the response of turbulence in non-equilibrium flows, the smooth wall and the two rough surfaces are placed in a channel with a three-fold step increase in mass flow rate at  $t^* = 0$ .

To validate the transient flow implementation, the “differential flow”—defined as the change of instantaneous velocity field from the initial field—is obtained as  $\hat{u}_i = u_i(x, y, z, t^*) - u_i(x, y, z, 0)$ , similar to He & Seddighi (2013), and is denoted by subscript “du”. The friction coefficient  $C_f$  and Reynolds number based on the momentum thickness,  $Re_\theta = U_b\theta/\nu$ , are obtained from the differential flow and compared with He & Seddighi (2013) in Fig. 8. Excellent agreement is obtained for the smooth case, with a dip in  $C_f$  indicating reverse transition to the laminar-like state due to strong acceleration. For both rough cases, however,  $C_f$  quickly recovers to the equilibrium value, without signs of stabilizing effect of acceleration.  $Re_\theta$  increases faster on the rough walls than the smooth one, consistent with the behavior of  $C_f$ .

The temporal variations of the peak values of wall-normal profiles of TKE and Reynolds shear stress are shown in Fig. 9. For the smooth case, the turbulence is “frozen” immediately after the step change, with the change of TKE lagging behind that of the mean flow, due to the slowly responding Reynolds shear stress and TKE production; the final equilibrium state is reached at  $t^* = 47$  (not shown). For the rough cases, the responses of Reynolds shear stress are much faster than in the smooth case. The topographical effects are manifested as a gradual adaptation of Reynolds shear stress to  $U_{b2}$  on TB, versus a nearly instantaneous re-

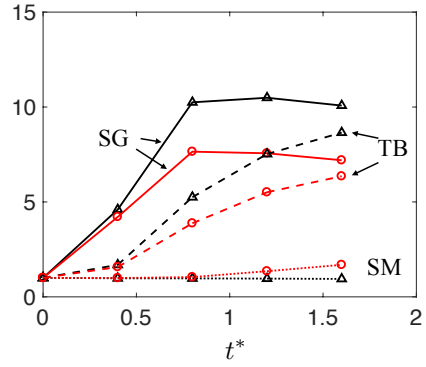


Figure 9. Variables of peak values of Reynolds shear stresses (black  $\triangle$ ) and TKE (red  $\circ$ ) in transient channels, normalized by  $u_\tau^2$  of the initial developed channel.

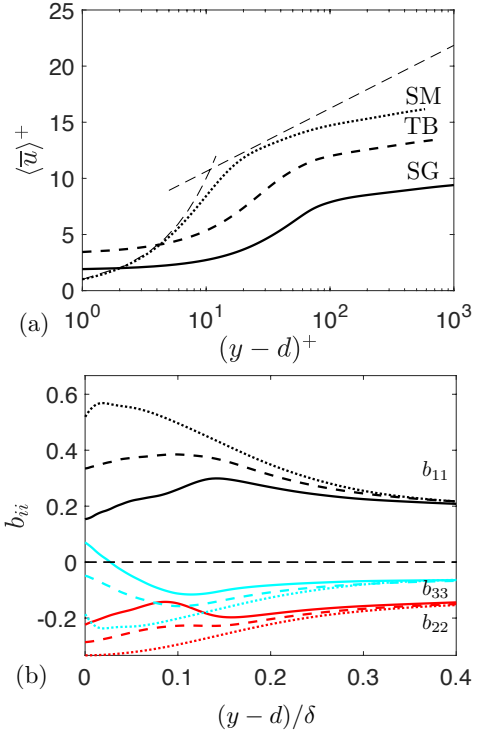


Figure 10. (a) Mean velocity and (b) Reynolds-stress anisotropy for all transient cases at  $t^* = 0.4$ .

sponse on SG.

A comparison of turbulent statistics at a time instance soon after the acceleration (at  $t^* = 0.4$ ) is shown in Fig. 10. The mean velocity profile in all cases exhibits a decrease of slope in the logarithmic region, consistent with numerous observation on spatial accelerating flows (e.g., Narasimha & Sreenivasan (1973), Spalart (1986)). Near the wall, the anisotropies are similar to the values in the equilibrium flow (Fig. 3), a sign that the roughness effects dominate the near-wall region, which has been also observed in spatially accelerating rough-wall boundary layer (Yuan & Piomelli, 2015). Nevertheless, for all cases in the region  $(y-d)^+ \approx 0.1 - 0.15$ , the acceleration leads to a tendency towards one-dimensional turbulence—as predicted by rapid distortion theory with strong mean shear,  $d\langle \bar{u} \rangle/dy$ —with a larger portion of TKE residing in the streamwise fluctuations (shown by a peak of  $b_{11}$  and the corresponding dips of

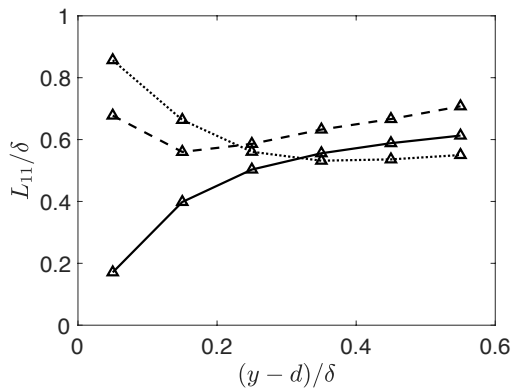


Figure 11. Integral length scale for all transient cases at  $t^* = 0.4$ .

$b_{22}$  and  $b_{33}$ ).

The integral length scales of  $u'$  motions at  $t^* = 0.4$  are compared among the three cases in Fig. 11. In contrast to the developed channel (Fig. 5), the accelerating channel over a smooth wall produces a peak of  $L_{11}$  near the wall, indicating that the streaks are elongated in this region by the strong mean shear during this period. Similarly, a weaker peak of  $L_{11}$  is also observed near the wall for TB, showing the sensitivity of turbulent structures on mean shear. However, on SG,  $L_{11}$  monotonically increases with the wall-normal distance, with a near-wall value of  $0.2\delta$ , insensitive to mean-flow distortion.

## CONCLUSIONS

Comparison of developed channel flows over a relatively uniform sandgrain roughness and a realistic roughness, with much wider range of length scales from  $0.1 - 5\delta$ , reveals several key effects of the surface textural details studied herein. (1) At the lower edge of the outer layer (where turbulence modeling typically requires correlating roughness parameters with turbulent scales), the integral length scale are affected by the surface, while similar velocity and time scales are produced by all surfaces, indicating that the near-wall turbulent scales are not sensitive to the large topographical lengths, which may play a role mainly in the distribution of the energetic turbulent motions, not in determining their intensity or dimensions. (2) Farther into the outer layer, however, the larger topographical scales appear to directly impact the energetic turbulent motions—which are now of the size of  $\delta$ —leading to larger and longer-lasting turbulent motions. (3) Inside the roughness sublayer, the roughness texture directly affects the dispersive stress distribution, and plays a role in determining the mean-momentum balance and turbulence production.

In transient channel flows, the flow behavior inside the roughness sublayer differs from the region above. (1) Away from the wall, the stabilizing effects of a strong acceleration is present for all surfaces, with the development of turbulence towards a one-dimensional state and elongation of coherent motions, consistent with the prediction of rapid distortion theory with strong mean shear. (2) Inside the roughness sublayer, the type of turbulence response is af-

ected by roughness topography, as the flow among sand grains appears insensitive to acceleration in terms of turbulence intensity and correlation length, while the turbulence among turbine roughness displays a slight increase of length scale, possibly because the large surface scales enable the development of regions of less disturbed flow that behaves similarly to the smooth-wall flow.

## ACKNOWLEDGMENTS

The author acknowledges the Office of Naval Research, program manager Thomas Fu, for the financial support of this research. Computational support was supplied by the Extreme Science and Engineering Discovery Environment (XSEDE), which is supported by National Science Foundation grant number ACI-1548562, and Michigan State University's High Performance Computing Facility.

## REFERENCES

- Cal, R. B., Brzek, B., Johansson, T.G. & Castillo, L. 2009 The rough favourable pressure gradient turbulent boundary layer. *J. Fluid Mech.* **641**, 129–155.
- He, S. & Seddighi, M. 2013 Turbulence in transient channel flow. *J. Fluid Mech.* **715**, 60–102.
- Jackson, P. S. 1981 On the displacement height in the logarithmic velocity profile. *J. Fluid Mech.* **111**, 15–25.
- Keating, A., Piomelli, U., Bremhorst, K. & Nešić, S. 2004 Large-eddy simulation of heat transfer downstream of a backward-facing step. *J. Turbul.* **5**, N20.
- Narasimha, R. & Sreenivasan, K. R. 1973 Relaminarization in highly accelerated turbulent boundary layers. *J. Fluid Mech.* **61**, 417–447.
- Nikuradse, J. 1933 Laws of flow in rough pipes. *NACA Technical Memorandum 1292*.
- Raupach, M. R. & Shaw, R. H. 1982 Averaging procedures for flow within vegetation canopies. *Bound.-Lay. Meteorol.* **22**, 79–90.
- Schultz, M. P. & Flack, K. A. 2013 Reynolds-number scaling of turbulent channel flow. *Phys. Fluids* **25**, 025104–1–13.
- Scotti, A. 2006 Direct numerical simulation of turbulent channel flows with boundary roughened with virtual sandpaper. *Phys. Fluids* **18**, 031701–1–4.
- Spalart, P.R. 1986 Numerical study of sink-flow boundary layers. *J. Fluid Mech.* **172**, 307–328.
- Wilcox, D. C. 2006 *Turbulence modeling for CFD*. DCW Industries.
- Yuan, J. & Piomelli, U. 2014a Estimation and prediction of the roughness function on realistic surfaces. Master's thesis, Queen's Uiversity.
- Yuan, J. & Piomelli, U. 2014b Numerical simulations of sink-flow boundary layers over rough surfaces. *Phys. Fluids* **26**, 015113–1–015113–28.
- Yuan, J. & Piomelli, U. 2014c Roughness effects on the reynolds stress budgets in near-wall turbulence. *J. Fluid Mech.* **760**, R1.
- Yuan, J. & Piomelli, U. 2015 Numerical simulation of a spatially developing accelerating boundary layer over roughness. *J. Fluid Mech.* **780**, 192–214.